JOURNAL OF GEOPHYSICAL RESEARCH: OCEANS, VOL. 118, 2535–2546, doi:10.1002/jgrc.20173, 2013

Annual maximum water levels from tide gauges: Contributing factors and geographic patterns

Mark A. Merrifield,[1] Ayesha S. Genz,[1] Christopher P. Kontoes,[1] and John J. Marra[2]

Received 14 August 2012; revised 26 January 2013; accepted 22 March 2013; published 20 May 2013.

[1] Hourly time series from a quasi-global set of 145 tide gauges are used to investigate annual maximum water levels at each station. High water levels are deconstructed into (1) a predicted tidal component, (2) a seasonal component, (3) a low-frequency nontidal residual that accounts for sea level variability at time scales greater than a month but less than a year, and (4) a high-frequency nontidal residual that captures variability particularly associated with storms at time scales greater than a month. The time-averaged annual maximum water level correlates significantly with, and scales as 2.5 times, the water level standard deviation at the tide gauge stations. This relationship is used to estimate time-averaged annual maximum water level on a nearly continuous global scale (excluding ice-covered polar regions) by specifying variance maps of the tides from a tide model, the seasonal and low-frequency residual components from satellite altimetry sea surface height, and the high-frequency residual component from an atmospheric reanalysis product. The variance fields are combined to estimate time-averaged annual maximum water levels that compare well with observed values at the tide gauge stations. Spatial patterns of annual maximum water levels and relative contributions from the tides and nontidal residual components are considered.

Citation: Merrifield, M. A., A. S. Genz, C. P. Kontoes, and J. J. Marra (2013), Annual maximum water levels from tide gauges: Contributing factors and geographic patterns, *J. Geophys. Res. Oceans*, *118*, 2535–2546, doi:10.1002/jgrc.20173.

1. Introduction

[2] High water level events pose an increasing concern for coastal communities given the current and projected rates of sea level rise. Extreme water level amplitudes have been observed to increase over time in tide gauge records, largely due to trends in mean sea level [*Woodworth and Blackman*, 2004; *Menéndez and Woodworth*, 2010; *Lowe et al*., 2010; *Seneviratne et al*., 2012]. The frequencies of extreme events also are likely to increase considerably over the course of the century with projected increases in global sea level [*Hunter*, 2012]. An understanding of the regional behavior of high water level events, and of the processes that contribute to them, is important for assessing future impacts.

[3] The most devastating atmospherically driven extreme events are due to storm surges caused by wind, wave, and atmospheric pressure forcing, such as in the Bay of Bengal [*Webster*, 2008; *Fritz et al*., 2009] and the Gulf of Mexico [*Fritz et al*., 2007]. In many coastal settings, the impacts of storm surges are strongly modulated by the tide. For example, the damage caused by an energetic storm event off San Francisco during the 1997–1998 El Niño was heightened because it peaked near high spring tides [*Ryan et al*., 1999]. In other areas, storm-driven residuals are weak and peak water levels occur primarily at spring tides, in which case the modulation of astronomical gravitational forcing determines the temporal variability of extreme events [*Pugh*, 1987; *Woodworth and Blackman*, 2004; *Haigh et al*., 2011]. For example, flooding events at the island nation of Tuvalu tend to occur during the largest spring tides of the year [*Hunter*, 2002], and coastal flooding has been reported in Hawaii when annual high spring tides coincide with water level anomalies of less than a few tens of centimeters [*Firing and Merrifield*, 2004].

[4] Tide gauges provide sea level time series with sufficient record lengths and sample periods to resolve extreme water levels over decade-to-century time scales. Although tide gauge stations typically are located in protected embayments, which limits the direct impact of wind waves relative to open coastlines [*Thompson and Hamon*, 1980], storm surges generally are well sampled by tide gauges. The value of tide gauge records for studying extreme water levels has been demonstrated in the context of the statistical probability of event occurrence [*Pugh and Vassie*, 1980], event reconstructions [*Bernier and Thompson*, 2006], the relationship of extreme events to climate indices [*Woodworth and Blackman*, 2004; *Menéndez and Woodworth*, 2010; *Sweet and Zervas*, 2011], changes in extreme events associated with changes in mean sea level [*Woodworth and Blackman*, 2002; *Menéndez and Woodworth*, 2010; *Lowe et al*., 2010] and with changes in storm activity [*Zhang et al*., 2000;

[1]Department of Oceanography, University of Hawaii at Manoa, Honolulu, Hawaii, USA.
[2]NOAA NESDIS National Climatic Data Center, Honolulu, Hawaii, USA.

Corresponding author: M. Merrifield, Department of Oceanography, University of Hawaii at Manoa, Marine Science Building 317, 1000 Pope Road, Honolulu, HI 96822, USA. (markm@soest.hawaii.edu)

2169-9275/13/10.1002/jgrc.20173

Table 1. Tide Gauge Station Names, International Country Codes (ISO-3166), Position, Record Start Year, Record Length in Years, and Time-averaged Annual Maxima at Each Station[a]

Station Name	Country	Lat.	Lon.	Start	Years	$\bar{h} \pm 2$ S.E. (cm)
Booby Is.	AUS	10.60°S	141.92°E	1988	20	199.8 ± 12.4
Brisbane	AUS	27.37°S	153.17°E	1984	26	151.5 ± 5.3
Broome	AUS	18.00°S	122.22°E	1992	18	499.5 ± 11.9
Bundaberg	AUS	24.83°S	152.35°E	1984	26	185.0 ± 7.1
Carnarvon	AUS	24.88°S	113.62°E	1989	16	106.1 ± 14.1
Cocos Is.	AUS	12.12°S	96.90°E	1986	21	90.5 ± 5.9
Darwin	AUS	12.47°S	130.85°E	1985	25	374.0 ± 6.9
Davis	AUS	68.45°S	77.97°E	1994	12	121.3 ± 11.5
Esperance	AUS	33.87°S	121.90°E	1985	24	98.7 ± 8.8
Fort Denison	AUS	33.85°S	151.23°E	1965	42	119.7 ± 4.6
Fremantle	AUS	32.05°S	115.73°E	1984	26	83.4 ± 9.4
Mawson	AUS	67.60°S	62.87°E	1993	13	91.0 ± 13.2
Port Hedland	AUS	20.32°S	118.57°E	1984	20	349.3 ± 11.8
Portland	AUS	38.34°S	141.61°E	1991	19	91.2 ± 7.3
Spring Bay	AUS	42.55°S	147.93°E	1985	23	89.2 ± 6.7
Thevenard	AUS	32.15°S	133.64°E	1998	12	172.7 ± 12.4
Townsville	AUS	19.25°S	146.83°E	1984	26	213.0 ± 11.7
Cananeia	BRA	25.02°S	47.93°W	1954	52	127.2 ± 6.1
Ilha Fiscal	BRA	22.90°S	43.17°W	1963	43	103.2 ± 8.5
Churchill	CAN	58.78°N	94.20°W	1962	39	258.5 ± 12.8
Halifax	CAN	44.67°N	63.58°W	1920	88	139.2 ± 5.5
Prince Rupert	CAN	54.32°N	130.33°W	1963	47	370.9 ± 8.4
St. John's	CAN	47.57°N	52.72°W	1993	16	115.1 ± 9.5
Tofino	CAN	49.15°N	125.92°W	1963	41	219.9 ± 9.4
Antofagasta	CHL	23.65°S	70.40°W	1946	56	91.4 ± 3.0
Caldera	CHL	27.07°S	70.83°W	1980	29	95.4 ± 3.4
Easter Is.	CHL	27.15°S	109.45°W	1970	29	70.5 ± 14.7
Juan Fernandez	CHL	33.62°S	78.83°W	1988	20	89.2 ± 4.5
Puerto Montt	CHL	41.48°S	72.97°W	1980	28	363.8 ± 10.4
Valparaiso	CHL	33.03°S	71.63°W	1944	54	107.0 ± 3.1
Penrhyn	COK	8.98°S	158.05°W	1978	29	35.8 ± 5.9
Rarotonga	COK	21.21°S	159.78°W	1993	17	59.4 ± 10.3
Baltra	ECU	0.44°S	90.29°W	1985	21	134.7 ± 7.0
La Libertad	ECU	2.20°S	80.92°W	1950	57	144.0 ± 4.3
Santa Cruz	ECU	0.75°S	90.31°W	1979	28	122.5 ± 4.5
Ceuta	ESP	35.90°N	5.32°W	1944	62	69.8 ± 2.8
La Coruna	ESP	43.37°N	8.40°W	1943	65	223.1 ± 4.8
Las Palmas	ESP	28.15°N	15.41°W	1991	18	145.9 ± 5.3
Lautoka	FJI	17.60°S	177.43°E	1993	17	114.4 ± 9.0
Suva	FJI	18.13°S	178.43°E	1998	12	97.7 ± 3.1
Brest	FRA	48.38°N	4.50°W	1846	149	373.7 ± 4.8
Kerguellen	FRA	49.35°S	70.22°E	1993	17	117.5 ± 5.1
Marseille	FRA	43.30°N	5.35°E	1985	12	58.8 ± 20.8
Kapingamarangi	FSM	1.10°N	154.78°E	1979	27	84.4 ± 4.7
Pohnpei	FSM	6.99°N	158.24°E	1975	35	86.4 ± 3.6
Yap	FSM	9.51°N	138.13°E	1969	36	88.4 ± 16.8
Bermuda	GBR	32.37°N	64.70°W	1985	20	85.9 ± 6.9
Lerwick	GBR	60.15°N	1.14°W	1959	46	140.1 ± 7.3
Newlyn	GBR	50.10°N	5.54°W	1915	92	295.3 ± 4.5
Stornoway	GBR	58.21°N	6.39°W	1978	27	271.5 ± 12.2
Quarry Bay	HKG	22.30°N	114.22°E	1986	24	152.9 ± 16.3
Abashiri	JPN	44.02°N	144.28°E	1968	41	94.5 ± 5.6
Aburatsu	JPN	31.57°N	131.42°E	1961	49	124.1 ± 9.9
Chichijima	JPN	27.10°N	142.18°E	1975	35	77.1 ± 8.6
Hakodate	JPN	41.78°N	140.73°E	1969	40	69.9 ± 4.3
Hamada	JPN	34.90°N	132.07°E	1984	26	67.5 ± 10.0
Ishigaki	JPN	24.33°N	124.15°E	1969	41	121.1 ± 14.6
Kushimoto	JPN	33.47°N	135.78°E	1961	47	107.8 ± 6.0
Kushiro	JPN	42.97°N	144.38°E	1965	44	84.3 ± 5.1
Maisaka	JPN	34.68°N	137.62°E	1968	40	89.6 ± 12.3
Mera	JPN	34.92°N	139.83°E	1968	41	91.8 ± 7.4
Nagasai	JPN	32.73°N	129.87°E	1985	25	163.8 ± 4.9
Naha	JPN	26.22°N	127.67°E	1967	43	124.1 ± 5.3
Nakano Sima	JPN	29.83°N	129.85°E	1984	26	131.1 ± 9.4
Nase	JPN	28.38°N	129.50°E	1957	49	124.2 ± 6.3
Nishinoomote	JPN	30.73°N	131.00E	1965	45	127.7 ± 5.9
Ofunato	JPN	39.07°N	141.72°E	1965	45	81.8 ± 5.0
Toyama	JPN	36.77°N	137.22°E	1967	43	47.9 ± 3.8
Wakkani	JPN	45.40°N	141.68°E	1967	43	51.1 ± 5.6
Lamu	KEN	2.27°S	40.90°E	1996	14	203.7 ± 5.8

Table 1. (continued)

Station Name	Country	Lat.	Lon.	Start	Years	$\bar{h} \pm 2$ S.E. (cm)
Betio	KIR	1.36°N	172.93°E	1994	16	128.2 ± 3.7
Christmas Is.	KIR	1.98°N	157.47°W	1974	32	62.4 ± 3.3
Kanton	KIR	2.81°S	171.72°W	1972	32	76.5 ± 4.5
Gan	MDV	0.69°S	73.15°E	1988	20	71.0 ± 2.7
Hulhule	MDV	4.18°N	73.53°E	1991	19	60.2 ± 3.0
Kwajalein	MHL	8.73°N	167.73°E	1946	63	106.6 ± 1.7
Majuro	MHL	7.11°N	171.37°E	1993	17	114.9 ± 4.9
Saipan	MHL	15.23°N	145.74°E	1979	24	54.5 ± 13.3
Port Louis	MUS	20.16°S	57.50°E	1987	23	54.0 ± 5.6
Rodrigues	MUS	19.67°S	63.42°E	1987	23	103.8 ± 11.9
Langkawi	MYS	6.43°N	99.77°E	1986	24	175.4 ± 5.9
Andenes	NOR	69.32°N	16.15°E	1992	18	147.7 ± 12.3
Rorvik	NOR	64.87°N	11.25°E	1970	38	179.1 ± 14.5
Tregde	NOR	58.00°N	7.57°E	1928	77	74.6 ± 5.4
Vardo	NOR	70.33°N	31.10°E	1948	36	194.0 ± 7.7
Bluff	NZL	46.60°S	168.33°E	1985	14	148.9 ± 6.2
Jackson	NZL	43.98°S	168.62°E	1999	11	156.1 ± 7.8
Wellington	NZL	41.28°S	174.78°E	1945	63	94.8 ± 3.7
Balboa	PAN	8.96°N	79.57°W	1908	98	298.8 ± 5.1
Callao	PER	12.05°S	77.15°W	1970	38	69.2 ± 3.6
Malakal	PLW	7.33°N	134.46°E	1971	37	103.9 ± 3.0
Lombrum	PNG	2.03°S	147.37°E	1996	14	51.7 ± 3.4
Papeete	PYF	17.53°S	149.57°W	1976	33	33.5 ± 7.1
Rikitea	PYF	23.13°S	134.95°W	1970	36	57.5 ± 2.8
Tanjong Pagar	SGP	1.26°N	103.85°E	1984	24	161.2 ± 8.3
Honiara	SLB	9.43°S	159.96°E	1995	15	55.6 ± 5.6
Stockholm	SWE	59.32°N	18.08°E	1889	119	59.9 ± 4.5
Pointe La Rue	SYC	4.67°S	55.53°E	1993	17	107.3 ± 6.5
Ko Lak	THA	11.80°N	99.82°E	1985	25	135.5 ± 8.7
Ko Taphao Noi	THA	7.83°N	98.43°E	1985	24	163.0 ± 4.8
Nuku'alofa	TON	21.13°S	175.17°W	1991	19	91.2 ± 5.8
Funafuti	TUV	8.53°S	179.20°E	1994	16	125.2 ± 5.8
Zanzibar	TZA	6.16°S	39.19°E	1984	25	246.8 ± 4.7
Adak Is.	USA	51.86°N	176.64°W	1950	50	114.9 ± 6.2
Atlantic City	USA	39.36°N	74.42°W	1912	91	145.8 ± 7.3
Charleston	USA	32.78°N	79.93°W	1922	85	146.7 ± 8.2
Crescent City	USA	41.75°N	124.18°W	1933	67	168.0 ± 6.1
Duck Pier	USA	36.18°N	75.74°W	1978	32	128.2 ± 11.9
Dutch Harbor	USA	53.88°N	166.54°W	1985	23	108.5 ± 7.5
Fort Pulaski	USA	32.03°N	80.90°W	1936	69	174.6 ± 5.4
Galveston	USA	29.31°N	94.79°W	1904	99	84.9 ± 15.1
Guam	USA	13.43°N	144.65°E	1948	55	51.3 ± 4.5
Hilo	USA	19.73°N	155.07°W	1927	68	70.3 ± 3.5
Honolulu	USA	21.31°N	157.87°W	1905	103	59.3 ± 1.8
Johnston Is.	USA	16.75°N	169.52°W	1947	54	74.8 ± 6.5
Kahului	USA	20.90°N	156.47°W	1951	52	64.7 ± 2.2
Kawaihae	USA	20.03°N	155.83°W	1990	17	66.4 ± 3.1
Ketchikan	USA	55.33°N	131.63°W	1919	65	357.0 ± 7.1
Key West	USA	24.55°N	81.81°W	1913	94	59.7 ± 4.0
Kodiak Is.	USA	57.73°N	152.51°W	1975	29	223.3 ± 11.8
La Jolla	USA	32.87°N	117.26°W	1925	77	134.1 ± 2.5
Midway Is.	USA	28.22°N	177.37°W	1947	55	62.0 ± 8.4
Mokuoloe	USA	21.43°N	157.80°W	1957	40	61.9 ± 3.0
Nawiliwili	USA	21.97°N	159.35°W	1955	55	58.7 ± 5.4
Neah Bay	USA	48.37°N	124.62°W	1935	73	199.8 ± 6.5
Newport	USA	41.51°N	71.33°W	1931	75	128.5 ± 7.4
Pago Pago	USA	14.28°S	170.68°W	1950	57	71.7 ± 2.1
Pensacola	USA	30.40°N	87.21°W	1923	83	72.6 ± 14.7
Prudhoe Bay	USA	70.40°N	148.53°W	1994	16	86.1 ± 23.3
San Diego	USA	32.72°N	117.17°W	1906	100	141.6 ± 2.3
San Francisco	USA	37.81°N	122.47°W	1898	112	132.9 ± 4.0
San Juan	USA	18.46°N	66.12°W	1978	30	49.6 ± 9.6
Seward	USA	60.12°N	149.43°W	1968	37	266.1 ± 9.6
Sitka	USA	57.05°N	135.34°W	1950	59	242.3 ± 7.6
South Beach	USA	44.63°N	124.04°W	1967	42	200.7 ± 8.8
Tern Is.	USA	23.87°N	166.29°W	1975	30	50.6 ± 4.9
Virginia Key	USA	25.73°N	80.16°W	1996	14	73.6 ± 11.5
Wake Is.	USA	19.28°N	166.62°E	1951	52	74.9 ± 8.5
Yakutat Bay	USA	59.55°N	139.74°W	1961	42	251.4 ± 8.5
Port Vila	VUT	17.77°S	168.30°E	1994	16	76.2 ± 5.6
Cape Town	ZAF	33.90°S	18.42°E	1968	25	115.7 ± 6.9
Port Elizabeth	ZAF	33.96°S	25.63°E	1979	22	126.6 ± 10.1

Table 1. (continued)

Station Name	Country	Lat.	Lon.	Start	Years	$\bar{h} \pm 2$ S.E. (cm)
Port Nolloth	ZAF	29.28°S	16.85°E	1959	35	120.3 ± 4.9
Saldahna Bay	ZAF	33.02°S	17.95°E	1974	20	113.4 ± 6.5
Simon's Bay	ZAF	34.18°S	18.43°E	1959	36	115.0 ± 4.9

[a]Data are reported with an uncertainty equal to two times the standard error. Station names in italics are those excluded from the linear regression depicted in Figure 2c.

Bromirski et al., 2003; *Bijl et al*., 1999; *Aucan et al*., 2012], and extreme event projections [*Cayan et al*., 2008; *Tebaldi et al*., 2012; *Hunter*, 2010, 2012].

[5] In this study, a quasi-global tide gauge data set is used to characterize patterns and forcing terms associated with the annual maximum water level relative to the annual mean at each tide gauge station. We use annual maxima given their simple interpretation and common usage for characterizing extreme water levels [e.g., *Mudersbach and Jensen*, 2010; *Bernier et al*., 2007]. The focus is on the time average of the annual maximum level over each tide gauge record. We seek to expand the spatial information on mean annual maximum water levels provided by the tide gauge network by using proxies for sea level variability provided by a global tide model, satellite altimetry data, and an atmospheric reanalysis product. Global maps are used to depict the relative contributions of tides and nontidal residuals to high annual water levels. Our study complements the event deconstruction approach of *Merrifield et al*. [2007] by using gridded proxies for water level variance to extrapolate between tide gauge stations.

2. Data and Methods

[6] Hourly time series from a quasi-globally distributed set of tide gauge stations were obtained from the University of Hawaii Sea Level Center (UHSLC) Research Quality database and extended through August 2010 using the UHSLC Fast Delivery database. The tide gauge locations and time series record lengths are listed in Table 1. The time series have not been corrected for the inverse barometer effect and so include the sea level response to atmospheric pressure changes. One hundred forty-five stations that meet the criterion of having at least 10 consecutive years of data with at least 80% data return annually are selected.

[7] For each tide gauge, we compile a time series, denoted here as h, of the annual maximum hourly water level above the annual mean. We treat a year as starting in April and ending the following March to keep the winter and summer seasons intact. Years with less than 80% data return are excluded from the analysis. By focusing on maxima relative to annual means, we do not consider the impacts of long-term trends and interannual variability and instead focus on factors that determine the average annual maximum level associated with tides, seasonal cycles, storms, and other oceanographic phenomena with time scales of less than 1 year.

[8] The identification of the annual maxima and the decomposition into tidal and residual contributions are illustrated for two tide gauge stations in the Pacific Ocean (Figure 1). At San Diego, the highest hourly water level relative to the annual mean (over 150 cm) occurred on 19 December 1968 during a perigean spring tide (Figure 1a). The nontidal residual contribution was ~30 cm. Over the course of many years, the h events at San Diego continue to occur at high tides with similar amplitude residual contributions (Figure 1b). San Diego is therefore a tidally dominated location in terms of contributions to h. In contrast, at Midway Atoll, the peak level (over 100 cm) on 12 January 1958 is associated with a rapid anomalous rise in sea level that is independent of the weak tidal range (Figure 1c). High residuals at Midway have been related to winter swell events that cause a setup of the atoll lagoon [*Aucan et al*., 2012]. The time series of h shows that extreme water levels at Midway are largely determined by these residual events with a smaller contribution from the tide (Figure 1d).

[9] We examine contributions to water level annual maxima in two ways. First, for each identified annual maximum in the tide gauge records, as depicted in Figure 1, we compute the associated predicted tidal component (h_p) and further subdivide the nontidal residual into the following three components: seasonal (h_s), low frequency (h_{lf}), and high frequency (h_{hf}). The seasonal cycle for a given tide gauge station is obtained from a least squares fit of annual and semi-annual frequency sinusoids to each year of data. The seasonal component, h_s, is the value of the seasonal cycle at the times of h. The harmonic tidal analysis program T_TIDE [*Pawlowicz et al*., 2002] is used to calculate the predicted tide for each year of record minus the seasonal cycle. The tidal component, h_p, is the predicted tide at the times of h. Predicting the tide each year minimizes timing errors that can lead to the leakage of tidal energy into the nontidal residual. The low-frequency residual is obtained by applying a running 1 month median filter to the hourly time series with the seasonal cycle, annual mean, and predicted tide removed. The median filter was used to account for positive skewness associated with storm-driven surge events at some stations. The low-frequency residual component, h_{lf}, is obtained from the median-filtered time series at the times of h. The high-frequency residual, h_{hf}, is the value of the annual maxima minus the annual mean, h_s, h_p, and h_{lf}. We consider the time averages of the annual maxima ($\bar{h}$) and each water level component ($\bar{h}_p$, $\bar{h}_s$, $\bar{h}_{lf}$, $\bar{h}_{hf}$) over all measurement years.

[10] In addition to decomposing high water level events in the manner illustrated in Figure 1, we also estimate the mean annual maximum water level at locations away from tide gauges using the variance of sea level, which is computed using proxies for tidal, seasonal, and low-frequency and high-frequency nontidal residual sea level variances. The contribution to the sea level variance made by the predicted tide is computed from tidal constituents provided by the TPXO8 tide model [*Egbert and Erofeeva*, 2002]. Specifically, we use the tidal constituents M_2, S_2, N_2, K_2, K_1, O_1, P_1, Q_1, and M_4 on a 1/30° resolution grid as well as M_f, M_m, MS_4, and MN_4 on a 1/6° resolution grid. We do not consider nodal and perigean tidal variations because our

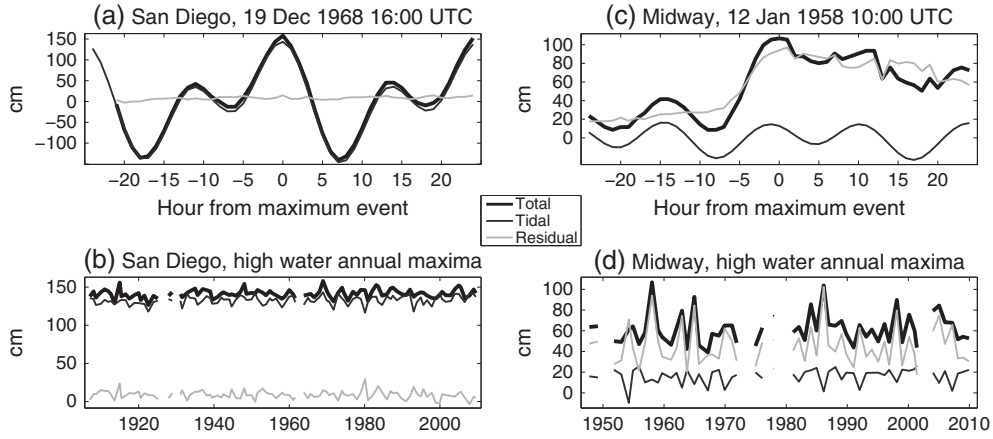

Figure 1. The highest water level events at (a) San Diego during 1967–1968 and (c) Midway during 1957–1958 are identified and separated into predicted tidal and nontidal residual components. Time series of total high water annual maximum, the tidal component, and the residual component indicate that on average (b) extremes at San Diego are dictated by the tide and (d) those at Midway by residuals.

focus is on the long-term time average of the annual maximum. The standard deviations of the predicted tidal elevation estimated from the tide gauge time series and the TPXO8 model, evaluated at model grid points nearest to each tide gauge station (Figure 2a), are highly correlated ($r = 0.99$). Linear regression analysis indicates that the tide gauge standard deviations are 1.03 ± 0.02 (error bars throughout indicate ± 2 X standard deviation) times higher

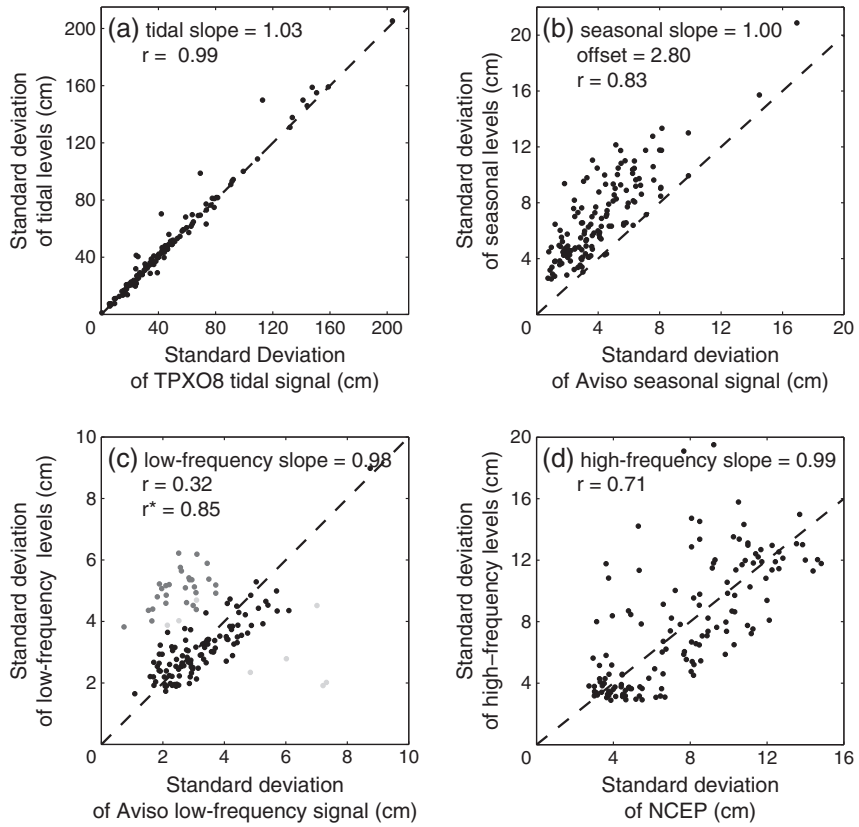

Figure 2. The relationship between tide gauge and proxy water level standard deviations is illustrated with scatter plots and correlation coefficients (r) for (a) the tide using the TPXO8 tide model, (b) the seasonal component using Aviso SSH, (c) the low-frequency residual using Aviso SSH ($r = 0.85$ excludes coastal stations indicated in gray, which are identified in Table 1), and (d) the high-frequency residual using NCEP reanalysis wind and atmospheric pressure. The regression slope assuming zero intercept is shown for each component, except for the seasonal component (Figure 2b), which has a significant offset term. All correlation coefficients are significantly different from zero at the 95% confidence level.

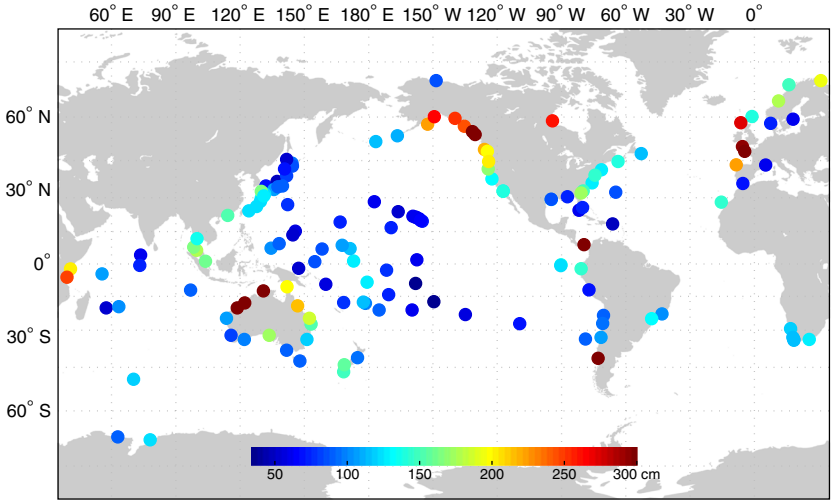

Figure 3. The mean annual maximum water level ($\bar{h}$) at each tide gauge station.

than the TPXO8 model standard deviations, which is attributed in part to the higher number of constituents used in the tide gauge predictions (~67) compared to the TPXO8 predictions (13). The TPXO8 predicted tidal elevation is multiplied by 1.03 to account for this difference.

[11] Satellite altimeter sea surface height (SSH) is used to specify gridded seasonal and low-frequency residual variances. Aviso altimeter SSH monthly data from December 1992 to December 2010 on a 0.25° resolution global grid were produced and distributed by Ssalto/Duacs with support from CNES (http://www.aviso.oceanobs.com/duacs). The standard deviation of the seasonal cycle is derived from annual and semi-annual sinusoids that are least squares fit to Aviso SSH (Figure 2b). The correlation between the standard deviations of the seasonal component estimated from the tide gauge data and from the SSH-based proxy is $r = 0.83$. The least squares regression slope is 1.00 ± 0.11. The seasonal component is the only one of four with a significant nonzero intercept, 2.80 ± 0.53 cm. The nature of the bias offset is not clear to us, but we include the small intercept correction in calculating the seasonal contribution to sea level variance.

[12] The variance of the low-frequency residual component is obtained from a high-pass filter of the SSH data (cutoff frequency = 1 cycle/year) with the seasonal cycle removed. High-latitude Aviso data impacted by seasonal ice formation are not included in the analysis. Low-frequency residual standard deviations are generally weak (<10 cm; Figure 2c), and the correlation with the tide gauge standard deviations is weak ($r = 0.32$). The least squares regression slope is 0.98 ± 0.07. The agreement between tide gauge and SSH low-frequency standard deviations improves considerably at open ocean island stations, with most discrepancies occurring at stations located at wide continental shelves (e.g., Northwest Shelf of Australia) or along irregular coastlines (e.g., Norway). For example, excluding 33 stations that share some of these characteristics (identified in Table 1) improves the correlation between tide gauge and SSH low-frequency standard deviations considerably ($r = 0.85$). In general, the low-frequency component is the weakest contributor to sea level variance in equation (1), and excluding this component does not lead to substantial changes in the results. Nevertheless, we include the low-frequency residual in our analysis because low-frequency standard deviations are relatively high at some tide gauge locations (e.g., Baltic Sea) and higher amplitudes are found at other locations where there are no tide gauge stations (e.g., western boundary current extension regions). We feel it is worth identifying these regions even if the tide gauges cannot provide direct validation of the results.

[13] To compute the high-frequency residual component, we use atmospheric surface pressure and wind speed from the NCEP1 reanalysis project [*Kalnay et al.*, 1996]. The daily surface pressure and wind data are obtained from 1992 to 2010 on a 2.5° resolution global grid. We apply a high-pass filter (cutoff frequency = 1 cycle/month) and calculate the variance at each ocean grid point. The variance of the pressure data is translated directly into water level variance assuming an inverse barometer relationship. High-frequency water level variance associated with wind speed is obtained by regressing wind speed on high-frequency water level with the inverse barometer correction applied. The regression coefficient then is used to scale wind variance to inverse barometer–corrected water level variance. The sums of the atmospheric pressure and wind speed variances are combined to obtain the high-frequency residual (Figure 2d). The correlation between the standard deviation of the high-frequency residual component estimated from the tide gauges and from the NCEP1-based proxy falls between the seasonal and low-frequency components ($r = 0.71$, slope $= 0.99 \pm 0.06$).

3. Results

[14] The long-term average of annual maximum water levels ($\bar{h}$) at each tide gauge station ranges from 33.5 to 499.5 cm (Figure 3 and Table 1). The $\bar{h}$ estimates generally are much larger than the standard errors of $\bar{h}$, which are computed from h assuming that an independent contribution to the mean is provided every 4.4 years (i.e., twice per lunar perigee cycle) (Table 1). Regions of high amplitude include the Northwest Shelf of Australia, the coasts of western Canada and southern Alaska, and Western Europe. Low amplitudes tend to occur at island stations in the central and western Pacific Ocean and in the Indian Ocean. Spatial patterns in $\bar{h}$ largely reflect the tidal contribution ($\bar{h}_p$), which

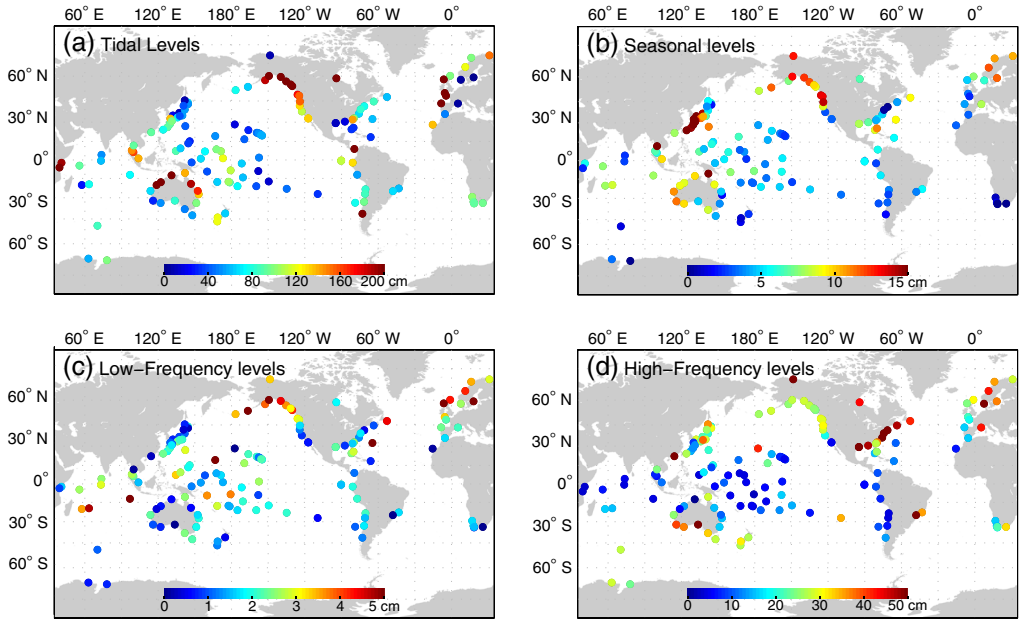

Figure 4. The average contributions to mean annual maximum water level ($\bar{h}$) at tide gauges associated with (a) the predicted tide ($\bar{h}_p$), (b) seasonal variations ($\bar{h}_s$), (c) low-frequency residual ($\bar{h}_{\mathrm{lf}}$), and (d) high-frequency residual ($\bar{h}_{\mathrm{hf}}$).

ranges from 0.3 to 476.2 cm (Figure 4a). The average seasonal contribution ($\bar{h}_s$) ranges between −0.6 and 29.2 cm, with high values in southern Japan, the coasts of western Canada and southern Alaska, western Australia, and Scandinavia (Figure 4b). The mean low-frequency residual contribution ($\bar{h}_{\mathrm{lf}}$) ranges from −2.9 to 10.9 cm, with high values at the coasts of western Canada and southern Alaska, northern Europe, and island stations in the southern Indian Ocean (Figure 4c). The mean high-frequency residual contribution ($\bar{h}_{\mathrm{hf}}$) ranges from −2.9 to 87.1 cm, with high values along the Atlantic coast of North America, northern Europe, and southern Australia (Figure 4d). For stations with at least 30 year record lengths, we find that the return period associated with $\bar{h}$ typically falls in the 2 to 3 year range based on a generalized extreme value analysis.

[15] The deconstruction approach provides an assessment of the contributions to annual maxima at the tide gauges, but it does not lend itself to estimates away from the tide gauge stations. We take advantage of the high correlation ($r = 0.99$) found between $\bar{h}$ and the standard deviation of water level at the tide gauges, σ (computed for frequencies ≥1 cycle/year) (Figure 5). A weighted linear regression of $\bar{h}$ onto σ, with the weights based on the uncertainties of $\bar{h}$ (listed in Table 1), yields a regression coefficient of 2.52 ± 0.05. We use this relationship to obtain a continuous map of $\bar{h}$ based on sea level variability, which we estimate using gridded data sets as proxies for the variability of the tidal, seasonal, and high-frequency and low-frequency residual components. That is, we seek an estimate of the average annual maximum water level at a given location based on

$$\bar{h} = 2.5\sqrt{\sigma_p^2 + \sigma_s^2 + \sigma_{\mathrm{lf}}^2 + \sigma_{\mathrm{hf}}^2} \qquad (1)$$

where the terms under the square root operator are the variances of the predicted tide, the seasonal component, and the low-frequency and high-frequency residuals, respectively. *Stockdon et al.* [2006] used a similar relationship to estimate wave-driven coastal water level maxima based on incident wave energy. Because each component in equation (1) represents a distinct range of frequencies in the sense of a Fourier series representation of variance, there are no covariance terms to consider. To the extent that the average annual maximum at a given station does result from a phase-locked superposition of inputs, i.e., if annual maxima tend to occur

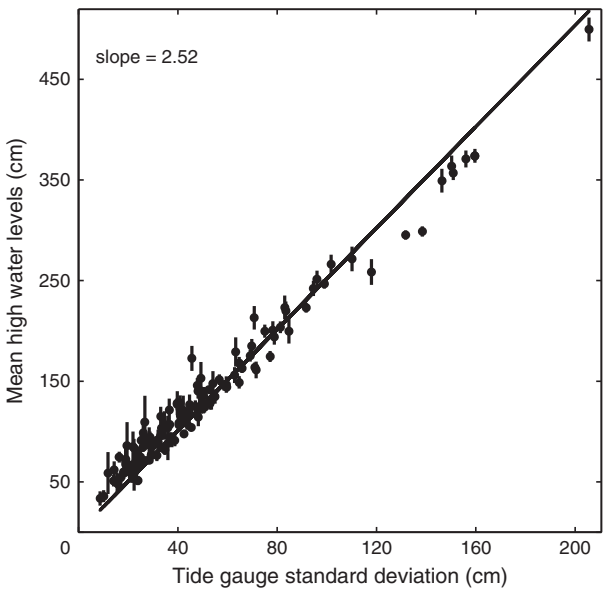

Figure 5. Scatter plot showing the high correlation ($r = 0.99$) between the standard deviation (σ) and the mean annual maximum water level ($\bar{h}$) derived from tide gauge station data. The least squares fit regression slope is 2.52 ± 0.05.

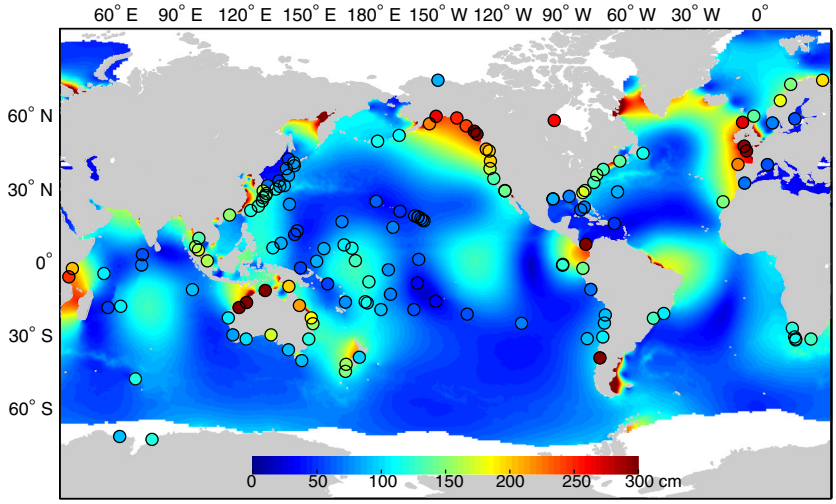

Figure 6. Predicted mean annual high water levels ($\bar{h}$) using equation (1) and the four water level components depicted in Figure 7. The equivalent $\bar{h}$ values obtained from the standard deviation of the tide gauge data are depicted by the colored circles.

when solstice high tides coincide with winter storms [e.g., *Merrifield et al.*, 2007], this dependent relationship would then be incorporated into the regression results presented in Figure 2. We do not attempt to distinguish spatial patterns of interdependencies in this study.

[16] The gridded proxy components are interpolated onto the 1/6° resolution TPXO8 grid and summed following equation (1) to form the mean annual maximum water levels ($\bar{h}$) (Figure 6). The estimated map of $\bar{h}$ shows similar spatial patterns as observed by the spatially sparse tide gauge network of stations (colored dots in Figure 6). To assess the uncertainty of the estimate of $\bar{h}$, the standard deviations of the individual variance components and of the regression coefficient in equation (1) are used to estimate twice the

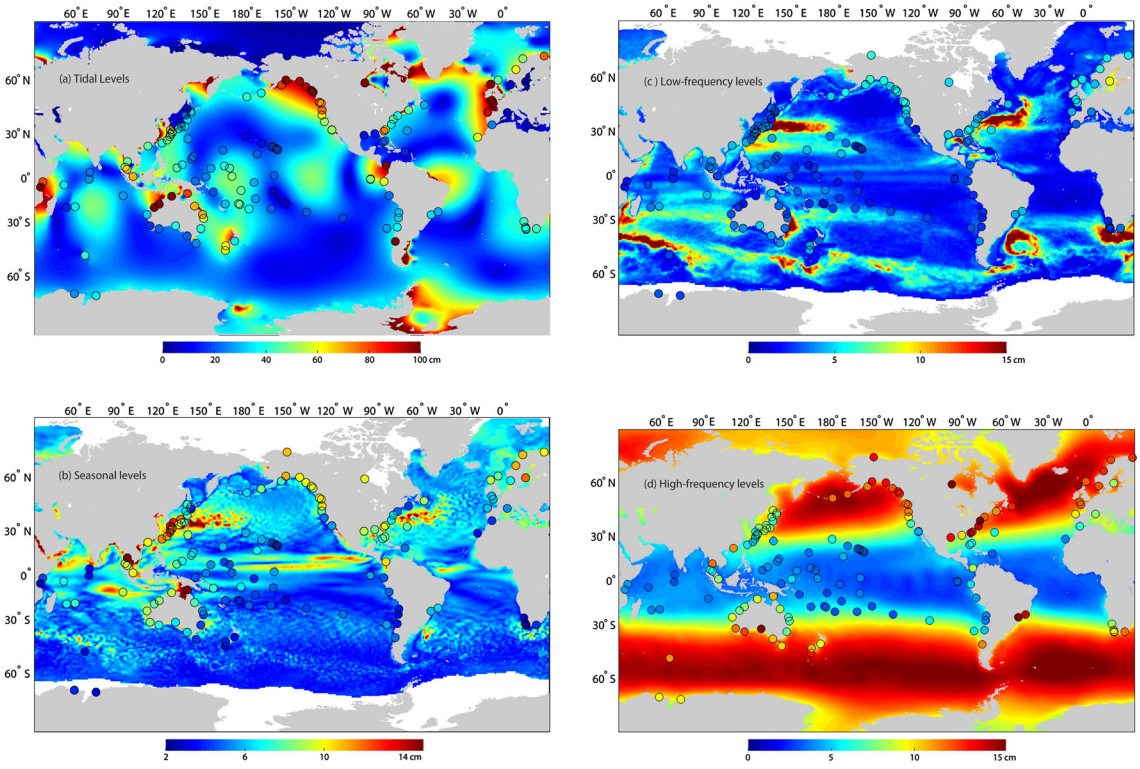

Figure 7. Estimated standard deviations for the components used to compute $\bar{h}$ (equation (1)), including (a) the predicted tidal component from TPXO8 (σ_p), (b) the seasonal component (σ_s) from Aviso SSH, (c) the low-frequency residual (σ_{lf}) from Aviso SSH, and (d) the high-frequency residual (σ_{hf}) obtained from NCEP1 reanalysis atmospheric pressure and surface wind data. The equivalent standard deviations obtained from the tide gauge data are depicted by the colored circles.

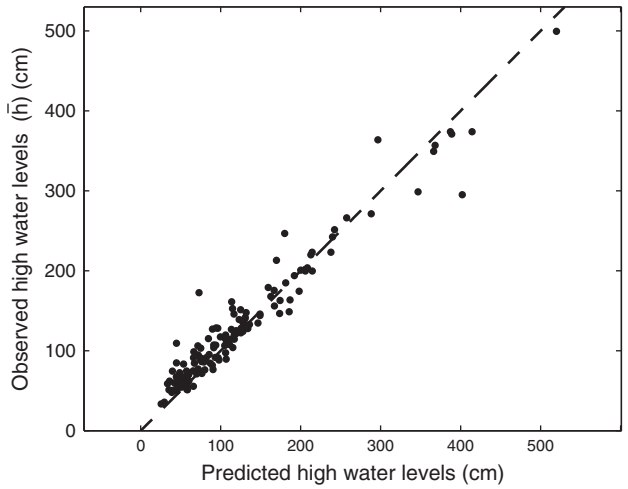

Figure 8. Scatter plot showing the predicted $\bar{h}$ from equation (1) using the water level proxies (Figure 7) and the observed $\bar{h}$ computed from the tide gauge data (Figure 3). The predicted $\bar{h}$ values are obtained by combining the components from the grid point closest to each tide gauge station, except for the high-frequency component, which is interpolated from the NCEP1 proxy grid.

standard deviation of $\bar{h}$. We do not include plots of these uncertainty maps because the values are small, on average 3% of $\bar{h}$, with no uncertainty larger than 27% of $\bar{h}$. The $\bar{h}$ uncertainties are small primarily because the estimated mean annual maxima are predominantly determined by the predicted tides (Figure 7a), consistent with the tide gauge deconstruction result (Figure 4a). The estimated and observed mean annual maxima at the tide gauge locations are highly correlated ($r = 0.97$) (Figure 8).

[17] The tidal, seasonal, and low-frequency and high-frequency residual standard deviation fields from the derived proxies (Figure 7) show similar spatial patterns as the mean contributions to annual maxima obtained by the deconstruction of the tide gauge records (Figure 4). The tidal component exhibits well-known features of the ocean tides, including mid-ocean amphidromic regions (elevation minima); high amplitudes along coastal boundaries due to Kelvin wave propagation, particularly in the eastern North Atlantic Ocean and North Pacific Ocean but also in the Bay of Bengal, Arabian Sea, and Sea of Okhotsk; and amplification in shallow coastal areas, such as the Bay of Fundy in eastern Canada, the Northwest Shelf of Australia, and the Mozambique Channel in the western Indian Ocean. The tide behaves as a quasi-standing wave in the tropics, with well-defined nodes and anti-nodes of elevation, particularly across the Pacific Ocean and Indian Ocean (Figure 7a). This standing pattern leads to significant tidal height variations between island groups in the western and central Pacific. Seasonal levels are high in western boundary current extensions, such as in the Kuroshio and Gulf Stream regions; in some semi-enclosed seas (e.g., Red Sea, Gulf of Carpentaria); as well as in the equatorial region (Figure 7b). Low-frequency levels are strongest in areas of strong eddy variability, such as the Kuroshio and Gulf Stream extension regions, the Antarctic Circumpolar Current, and the Agulhas Current (Figure 7c). These high eddy energy regions generally do not extend into adjacent coastal zones at the tide gauge stations. High-frequency levels are high in the main extratropical storm regions of the North Pacific Ocean and North Atlantic Ocean and the Southern Ocean (Figure 7d).

[18] We next identify regions where the mean annual maximum water level is dominated by the tide as opposed to nontidal residuals. The relative importance of tides to high water levels is summarized by the ratio,

$$\gamma = \bar{h}/(2.5\sigma_p). \tag{2}$$

Where $\gamma = 1$, the tides entirely determine the mean annual maximum level by equation (1). Where γ exceeds 1, nontidal residuals contribute to the annual maxima. For example, a value of $\gamma = 1.5$ implies that nontidal residuals combine to give a mean annual maximum that is 50% higher than what would be expected from the tide alone.

[19] Regions of large γ (Figure 9 and Table 1) include the main tidal amphidromes where the tidal elevation amplitudes

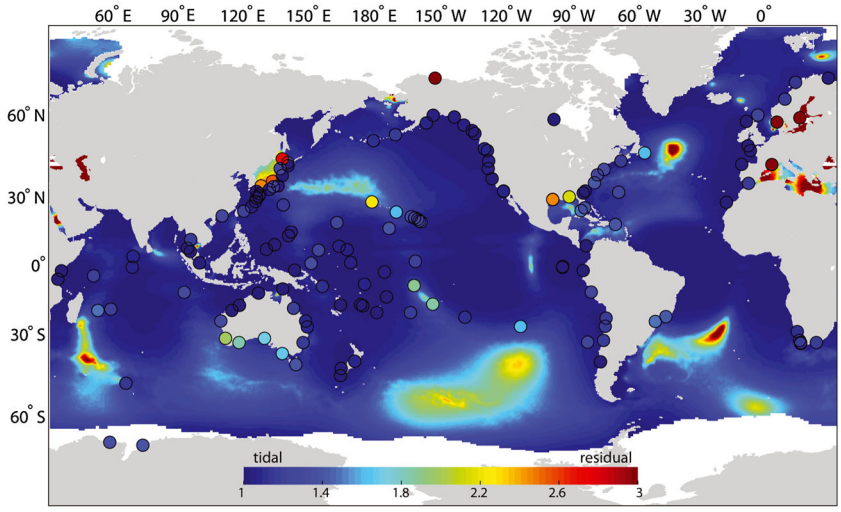

Figure 9. The ratio of mean annual maximum water levels to 2.5 times the standard deviation of the predicted tidal elevation standard deviation ($\gamma = \bar{h}/(2.5\sigma_p)$) provides an indication of regions where $\bar{h}$ tends to be tidally dominated (blue) and residually dominated (red).

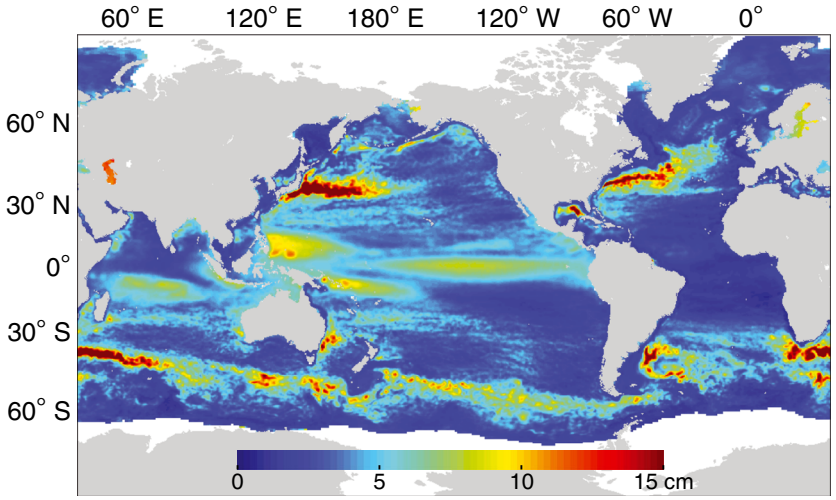

Figure 10. The standard deviation of low-frequency water level (frequencies <1 cycle/year) obtained from Aviso monthly SSH data.

are weak (see Figure 7a). These amphidromes are prominent in the Southern Ocean and in the central North Pacific Ocean and Atlantic Ocean. Tidal elevations are also weak, as are the tidal contributions to annual maxima, in the Mediterranean Sea, the Gulf of Mexico and the Caribbean, the Red Sea, and the Sea of Japan. Locations where high water levels are strongly tidally driven include the Northwest Shelf of Australia, where semidiurnal tides have a large range; at scattered islands in the Pacific Ocean; on the coast of eastern Africa; and along much of the eastern Pacific. There are notable regional variations in γ, such as the west (more tidal) versus east (more residual) coasts of North America, the United Kingdom (tidal) versus Scandinavia (residual), and the northern (tidal) versus southern (residual) coasts of Australia. As in the case of $\bar{h}$, the estimated uncertainties of γ, not shown, are weak, with an average value of 3% of γ, with no value greater than 27% of γ.

[20] The sense of tidal versus storm-dominated water level maxima inferred from Figure 9 is consistent with station-specific findings from previous studies. For example, *Woodworth and Blackman* [2004] found that Stockholm, Sweden (59.32°N, 18.08°E), is mostly surge (nontidal) dominated, whereas Funafuti, Tuvalu (8.38°S, 179.22°E), is tidally dominated. *Bromirski et al.* [2003] noted a general increase in extreme nontidal sea level (storminess) from Southern California to Northern California. *McInnes et al.* [2009] highlighted the importance of storm surges along the southeast coast of Australia. *Thompson and Mitchum* [2012] examined storm-driven extremes along the east coast of North America, and *Aucan et al.* [2012] described Midway as having strong wave-related extreme water levels. Our proxy for high-frequency residual variability does not explicitly include the effects of distant swell forcing, so the correspondence between the tide gauge results and the proxy reconstruction at Midway is somewhat coincidental, except to note that the tidal range at Midway is relatively small, thus raising the importance of residual forcing no matter the cause.

[21] We have focused on annual maxima relative to the annual mean and considered the time-averaged component. As a result, the contributions of interannual sea level fluctuations are not a factor in this analysis. To give a sense of the magnitude of interannual fluctuations relative to the mean annual maxima, we consider the standard deviation of the low-pass filtered (cutoff period = 1 year) SSH (Figure 10). Interannual sea level fluctuations with standard deviations >10 cm occur in regions of high eddy activity (western boundary current extension regions, ACC fronts) and El Niño and La Niña variability (tropical Indo-Pacific). In years of peak interannual levels, we would anticipate water levels of two to three times the standard deviations shown in Figure 10 to contribute to the annual maxima.

4. Summary and Discussion

[22] We have considered a geographic description of mean annual maximum water levels and assessed how different processes contribute to these maxima. The tides largely dictate the mean annual maximum level at most locations, and in tidally dominated regions the highest water level of the year will tend to occur at spring tides with weaker water level contributions from nontidal residuals. In regions that are considered strongly tidal (dark blue zones in Figure 9), the timing of the extreme will mostly likely occur at the highest spring tides of the year during solstices or equinoxes [*Pugh*, 1987; *Merrifield et al.*, 2007]. The annual maxima in tidally dominated areas can be expected to be ~2.5 times the standard deviation of the tidal elevation, which is equivalent to ~1.5 times the more common measure of tidal range, the mean higher high water (average of the tidal daily maxima). Moreover, interannual variations in tidally dominated extremes are expected to follow the 18.61 year nodal cycle and the ~4.4 year perigean cycle [*Woodworth and Blackman*, 2004; *Menéndez et al.*, 2009].

[23] High water level events associated with nontidal residual elevations tend to dominate in zones of weak tidal range (e.g., the Mediterranean), especially strong storm forcing (e.g., south coast of Australia), or both (e.g., Gulf of Mexico). The combination of tidal and residual forcing leads to notable regional variations in high water levels (Figure 9), for example, along the coastlines of Australia

(north versus south coasts), North America (east versus west coasts), and Europe (open ocean sites versus marginal seas).

[24] Energetic storm surges associated with tropical and extratropical storms are not well represented in this analysis. The tide gauge records generally are not long enough to measure adequately the statistics of extreme cyclone surge events, and our proxy for high-frequency variability based on NCEP reanalysis atmospheric pressure and winds does not resolve cyclone variability in detail. While the impact of tropical storms on the average annual maxima may not be large given that intense storm landfalls at a given tide gauge station generally occur infrequently, we note that when considering lower probability extreme events with more damaging consequences, the influence of tropical cyclones, as well as intense extratropical storms in general, will require greater scrutiny than given in this study.

[25] We note that in developing our regression fits for high-frequency residual variability at tide gauges, we did not take into account that surge amplitudes at a continental margin may be far larger than those along an island coastline and certainly higher than the storm response in the open ocean. In this regard, the high-frequency residual contribution to $\bar{h}$ is likely biased high in the open ocean and perhaps along island shorelines and may be biased low along continental shorelines with strong wind-forced surges [e.g., *Webster*, 2008; *Fritz et al*., 2009].

[26] The methodology used here can be extended in a number of ways. Global maps of sea level rise projections or of sea level patterns associated with climate modes of variability can be added to Figure 6 to give a sense of how the mean annual maxima may change over longer time scales. Projected changes in storm characteristics or atmospheric state can be incorporated into projections of annual maxima by adjusting the high-frequency contribution to sea level variance (Figure 7d). In addition, wave-driven coastal water level effects (e.g., wave setup) can be added as an additional contribution to water level variance, although validation of this component will require water level measurements in areas directly impacted by ocean waves.

[27] Lastly, we emphasize that the results presented here pertain to high-probability extreme events, i.e., those associated with 2 to 3 year return periods. Events in this probability range are dictated strongly by the tides. Less probable events, such as a 50 year return period event, will be determined primarily by extreme storm surge events and less so by the tides and other factors. Assessments of low probability extreme events will require better proxies for storm forcing than considered in this study.

[28] **Acknowledgments.** This work was funded as part of the NOAA NOS Coastal Storms Project and NCDC Pacific Storms Climatology Products Project via a grant from the East West Center. Additional support was provided by the NOAA Office of Climate Observations (award NA09OAR4320075). Insightful criticisms from three anonymous reviewers led to numerous improvements to the manuscript. We thank Shikiko Nakahara for assistance in constructing and processing the various data sets used in this analysis.

References

Aucan, J., R. Hoeke, and M. A. Merrifield (2012), Wave-driven sea level anomalies at the Midway tide gauge as an index of North Pacific storminess over the past 60 years, *Geophys. Res. Lett.*, *39*(17), doi:10.1029/2012GL052993.

Bernier, N. B., and K. R. Thompson (2006), Predicting the frequency of storm surges and extreme sea levels in the northwest Atlantic, *J. Geophys. Res.*, *111*, C10009, doi:10.1029/2005JC003168.

Bernier, N. B., K. R. Thompson, J. Ou, and H. Ritchie (2007), Mapping the return periods of extreme sea levels: Allowing for short sea level records, seasonality, and climate change, *Global Planet. Change*, *57*(1–2), 139–150.

Bijl, W., R. Flather, J. G. de Ronde, and T. Schmith (1999), Changing storminess? An analysis of long-term sea level data sets, *Climate Res.*, *11*, 161–172.

Bromirski, P. D., R. E. Flick, and D. R. Cayan (2003), Storminess Variability along the California Coast: 1858–2000, *J. Clim.*, *16*, 982–993.

Cayan, D., P. Bromirski, K. Hayhoe, M. Tyree, M. Dettinger, and R. Flick (2008), Climate change projections of sea level extremes along the California coast, *Clim. Chang.*, *87*, 57–73.

Egbert, G., and S. Erofeeva (2002), Efficient inverse modeling of barotropic ocean tides, *J. Atmos. Oceanic Technol.*, *19*, 183–204.

Firing, Y. L., and M. A. Merrifield (2004), Extreme sea level events at Hawaii: Influence of mesoscale eddies, *Geophys. Res. Lett.*, *31*, L24306, doi:10.1029/2004GL021539.

Fritz, H. M., C. Blount, R. Sokoloski, J. Singleton, A. Fuggle, B. G. McAdoo, A. Moore, C. Grass, and B. Tate (2007), Hurricane Katrina storm surge distribution and field observations on the Mississippi barrier islands, *Estuar. Coast. Shelf Sci.*, *74*, 12–20.

Fritz, H. M., C. D. Blount, S. Thwin, M. K. Thu, and N. Chan (2009), Cyclone Nargis storm surge in Mynamar, *Nat. Geosci.*, *2*, 448–449.

Haigh, I. D., M. Eliot, and C. Pattiaratchi (2011), Global influences of the 18.61 year nodal cycle and 8.8 year cycle of lunar perigee on high tide levels, *J. Geophys. Res.*, *116*, C06025, doi:10.1029/2010JC006645.

Hunter, J. R. (2002), A Note on Relative Sea Level Change at Funafuti, Tuvalu, edited, p. 22, Antarctic Cooperative Research Centre, University of Tasmania, Tasmania, Australia.

Hunter, J. (2010), Estimating sea level extremes under conditions of uncertain sea level rise, *Clim. Chang.*, *99*, 331–350.

Hunter, J. (2012), A simple technique for estimating an allowance for uncertain sea-level rise, *Clim. Chang.*, *113*(2), 239–252.

Kalnay, E., et al. (1996), The NCEP/NCAR 40-year reanalysis project, *Bull. Am. Meteorol. Soc.*, *77*(3), 437–470.

Lowe, J. A., et al. (2010), Past and future changes in extreme sea levels and waves, in *Understanding Sea-Level Rise and Variability*, 1st edition, edited by J. A. Church et al., 326–375, Wiley-Blackwell, West Sussex, UK.

McInnes, K. L., I. Macadam, G. D. Hubbert, and J. G. O'Grady (2009), A modelling approach for estimating the frequency of sea level extremes and the impact of climate change in Southeast Australia, *Nat. Hazards*, *51*, 115–137.

Menéndez, M., F. J. Mendez, and I. J. Losada (2009), Forecasting seasonal to interannual variability in extreme sea levels, ICES, *J. Mar. Sci.*, *66*, 1490–1496.

Menéndez, M., and P. L. Woodworth (2010), Changes in extreme high water levels based on a quasi-global tide-gauge data set, *J. Geophys. Res.*, *115*, C10011, doi:10.1029/2009JC005997.

Merrifield, M. A., Y. L. Firing, and J. J. Marra (2007), Annual Climatologies of Extreme Water Levels, paper presented at Extreme Events: Proceedings 15th 'Aha Huliko'a Hawaiian Winter Workshop, University of Hawaii at Manoa, Honolulu, HI.

Mudersbach, C., and J. Jensen (2010), Nonstationary extreme value analysis of annual maximum water levels for designing coastal structures on the German North Sea coastline, *J. Flood Risk Management*, *3*(1), 52–62.

Pawlowicz, R., B. Beardsley, and S. Lentz (2002), Classical Tidal Harmonic Analysis Including Error Estimates in MATLAB using T_TIDE, *Comp. Geosci.*, *28*, 929–937.

Pugh, D. T. (1987), *Tides, Surges and Mean Sea-Level: A Handbook for Engineers and Scientists*, pp. 472, John Wiley & Sons, Chichester.

Pugh, D. T., and J. M. Vassie (1980), Applications of the joint probability method for extreme sea level computations, *Proc. Instn Civil Engrs, Part 2*, *69*, 959–975.

Ryan, J., H. Gibbons, J. W. Hendley II, and P. Stauffer (1999), El Niño Sea-Level Rise Wreaks Havoc in California's San Francisco Bay Region, *U.S. Geological Survey Fact Sheet*, *175–99*, 4.

Seneviratne, S., et al. (2012), *Changes in climate extremes and their impacts on the natural physical environment, Managing the risks of extreme events and disasters to advance climate change adaptation (SREX)*, pp. 109–230, IPCC, Cambridge.

Stockdon, H. F., R. A. Holman, P. A. Howd, and A. H. Sallenger, Jr. (2006), Empirical parameterization of setup, swash, and runup, *Coast. Eng.*, *53*, 573–588.

Sweet, W. V., and C. Zervas (2011), Cool-season sea level anomalies and storm surges along the U. S. East Coast: Climatology and comparison with the 2009–10 E Nino, *Mon. Weather Rev.*, *139*, 2290–2299.

Tebaldi, C., B. H. Strauss, and C. E. Zervas (2012), Modelling sea level rise impacts on storm surges along US coasts, *Environ. Res. Lett.*, *7*, doi:10.1088/1748-9326/7/1/014032.

Thompson, P. T., and G. T. Mitchum (2012), Variability of winter storminess in the eastern United States during the 20th century from tide gauges, *J. Clim.*, submitted.

Thompson, R. O. R. Y., and B. V. Hamon (1980), Wave setup of harbor water levels, *J. Geophys. Res.*, *85*(C2), 1151–1152.

Webster, P. J. (2008), Myanmar's deadly daffodil, *Nat. Geosci.*, *1*, 488–490.

Woodworth, P. L., and D. L. Blackman (2002), Changes in extreme high waters at Liverpool since 1768, *Int. J. Climatol.*, *22*(6), 697–714.

Woodworth, P. L., and D. L. Blackman (2004), Evidence for Systematic Changes in Extreme High Waters since the Mid-1970s, *J. Clim.*, *17*, 1190–1197.

Zhang, K., B. C. Douglas, and S. P. Leatherman (2000), Twentieth-Century Storm Activity along the U.S. East Coast, *J. Clim.*, *13*, 1748–1761.